



DATA PAPER

Open Access



UruDendro, a public dataset of 64 cross-section images and manual annual ring delineations of *Pinus taeda* L.

Henry Marichal^{1*} , Diego Passarella² , Christine Lucas⁴ , Ludmila Profumo³ , Verónica Casaravilla³ , María Noel Rocha Galli³, Serrana Ambite⁴ and Gregory Randall¹ 

Key Message The automatic detection of tree-ring boundaries and other anatomical features using image analysis has progressed substantially over the past decade with advances in machine learning and imagery technology, as well as increasing demands from the dendrochronology community. This paper presents a publicly available dataset of 64 annotated images of transverse sections of commercially grown *Pinus taeda* L. trees from northern Uruguay, presenting 17 to 24 annual rings. The collection contains several challenging features for automatic ring detection, including illumination and surface preparation variation, fungal infection (blue stains), knot formation, missing bark or interruptions in outer rings, and radial cracking. This dataset can be used to develop and test automatic tree ring detection algorithms. The dataset presented here was used to develop the Cross-Section Tree-Ring Detection (CS-TRD) method, an open-source automated ring-detection algorithm for cross-sectioned images. Dataset access at <https://doi.org/10.5281/zenodo.15110647>. Access to the metadata describing the data set: <https://metadata-afs.nancy.inra.fr/geonetwork/srv/fre/catalog.search#/metadata/5fdbd411-9ae1-4ce6-8ef0-cdfa2fbd7a6a>.

Keywords Image processing, Tree ring area, Tree ring width, Wood cross sections, Dendrometry, Automatic measurement

1 Background

There is a global effort to digitize tree rings and automate ring-width measurements. A growing number of open tree-ring data sets with site-scale metadata and ring-width measurements are available. Still, many of those

datasets lack the accompanying images. This makes it challenging to use them to analyze tree-ring attributes further or develop new tree-ring detection algorithms based on images. Notably, deep learning algorithms for tree ring delineation require such image data (Poláček et al. 2023; Kim et al. 2023; Shi et al. 2019; Fabijańska and Danek 2018; Gillert et al. 2023). Additionally, experts must manually annotate images, which is time-consuming and expensive.

Few publicly available wood cross-section images with annual ring annotations exist, which is essential for developing such automatic methods. To our knowledge, there are only two: Kennel et al. (2015) who presented a publicly available dataset comprising seven images of *Picea glauca* (Moench) Voss and Gillert et al. (2023) who presented a dataset of microscopy images composed of *Dryas octopetala* L., *Empetrum nigrum* ssp.

Handling editor: Irène Gabriel.

*Correspondence:

Henry Marichal
hmarichal93@gmail.com

¹ Instituto de Ingeniería Eléctrica, Facultad de Ingeniería, Universidad de la República, Montevideo, Uruguay

² Sede Tacuarembó, CENUR Noreste, Universidad de la República, Montevideo, Uruguay

³ Sede Rivera, CENUR Noreste, Universidad de la República, Montevideo, Uruguay

⁴ Sede Paysandú, CENUR Litoral Norte, Universidad de la República, Montevideo, Uruguay



© The Author(s) 2025. **Open Access** This article is licensed under a Creative Commons Attribution 4.0 International License, which permits use, sharing, adaptation, distribution and reproduction in any medium or format, as long as you give appropriate credit to the original author(s) and the source, provide a link to the Creative Commons licence, and indicate if changes were made. The images or other third party material in this article are included in the article's Creative Commons licence, unless indicated otherwise in a credit line to the material. If material is not included in the article's Creative Commons licence and your intended use is not permitted by statutory regulation or exceeds the permitted use, you will need to obtain permission directly from the copyright holder. To view a copy of this licence, visit <http://creativecommons.org/licenses/by/4.0/>.

hermaphroditum (Hagerup) Böcher, and *Vaccinium myrtillus* L. species with 213 delineated samples (1987 rings).

This work aims to contribute to the community a public database of *P. taeda* from Uruguay, including 64 cross-sectional images and expert-traced tree ring

annotations on those images. Stem cross-sections were required to detect ring width variations throughout the cross-section. Figure 1 illustrates some image samples from the dataset.

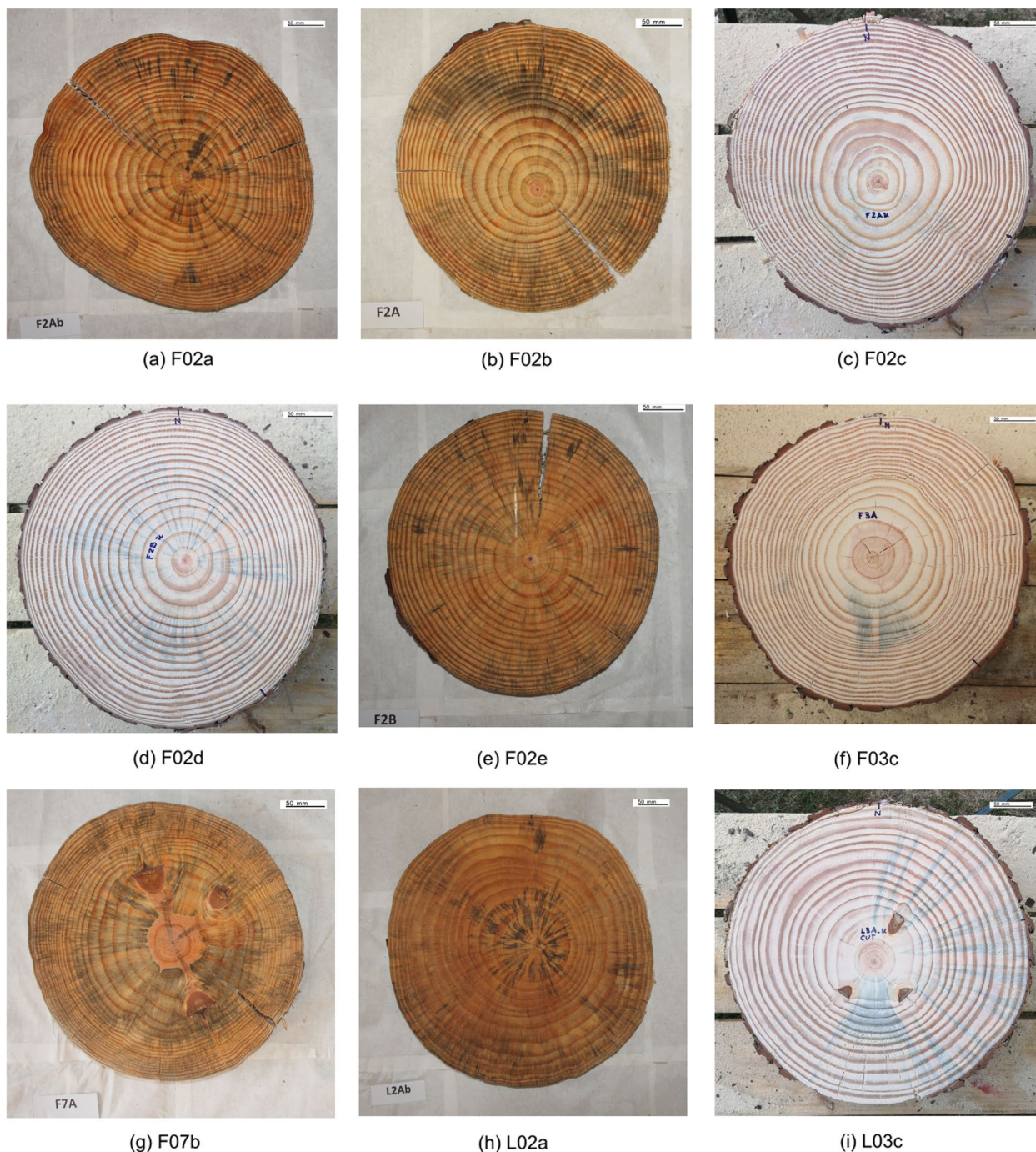


Fig. 1 Nine representative examples of the 64 images in the UruDendro data set. Note the variability in color, contrast, the presence of fungus (e.g., image L02a), knots (e.g., images F07b and F03c), and cracks (e.g., images F02e and L03c). The first five images are from the same tree taken at multiple heights

2 Methods

2.1 Image acquisition

Fourteen trees of *P. taeda* were collected in February 2020 from two tree plantations located in Buena Unión, Rivera, in northeastern Uruguay (Plywood company stands: 31°17'45" S 55°41'42" W; Lumber company stands: 31°10'4" S 55°39'42" W). This region has a humid subtropical climate—*Cfa*, Köppen Climate Classification (Beck et al. 2018)—with a mean annual rainfall of 1472 ± 373 mm/year (mean ± standard deviation), ranging from 830 to 2797 mm annually and a mean annual temperature of 17.2 ± 0.4 according to publicly available climate data from the National Institute of Agricultural Research (INIA) Tacuarembó meteorological station, for the years 1978 to 2022 (INIA 2023). Soils in both stands are comprised of sandstone (*areniscas* in Spanish) and pertain to the national soil classes 7.2 and 7.31 according to the *Comisión Nacional de Estudio Agronómico de la Tierra* (CO.N.E.A.T.) system. Soil type 7.2 is considered a Tacuarembó sandstone with a slope of 10–15 degrees and deep soils with very good drainage. Soil type 7.31 is also a Tacuarembó sandstone with a 6–10 degree slope and good drainage. Prevailing winds are, in order of importance, from the southwest, east, south, and southeast, with an average intensity of 15 to 20 km/h.

Seven trees were harvested from tree plantations managed by a lumber company (denoted with the letter F) and seven by a plywood company (denoted by the letter L). Each company applied different silvicultural practices summarized in Table 1. Cross-sections between 5 and 20 cm thick were cut from logs at 10, 165, 200, 400, and 435 cm above ground, totaling 64 cross-sections (1 to 5 cross-sections per tree). The image of each cross-section was assigned an identification code comprising the letter indicating the company (F or L), a two-digit number corresponding to the individual, and a lowercase letter corresponding to the height where each cross-section was cut. Height codes were as follows: *a* = 10 cm, *b* = 165

cm, *c* = 200 cm, *d* = 400 cm, and *e* = 435 cm above ground.

The cross-sections were dried at room temperature without further preparation. Due to the drying process, radial cracks and blue fungus stains appeared in many samples. Surfaces were polished with a handheld planer and a rotary sander from 60- to 1000-grain sandpaper. Photographs were taken under different lighting conditions; cross-sections *a*, *b*, and *e* were photographed indoors with an iPhone 6S cell phone (RGB sensor of 12 Mpx), moistening the surface to maximize the contrast between early and late wood. In contrast, photographs of dry cross-sections *c* and *d* were taken outdoors with a Huawei P20 Pro cell phone (RGB sensor Leica Vario-Summilux of 40 Mpx). For each disc, the north side of the tree was marked. Figure 1 shows a subset of images, representing variability in sample quality within the database. A black scale bar representing 50 mm was added to the upper right corner, based on the pixel-to-millimeter ratio described in Sect. 2.3. Additionally, the image background was manually removed using the GIMP tool (2025), while preserving the bark.

Table 2 summarizes the dataset’s main characteristics, comprising 64 images. As mentioned, the ID code for each image corresponds to the company, the specific tree, and the height at which samples were cut. The second column indicates the total number of experts who annotated each image (details in Sect. 2.2). The third column shows the number of annual rings, while the fourth specifies the year of the first detected growth ring in the section. The final two columns represent the image height and width in pixels, respectively.

2.2 Manual ring tracing

Experts manually traced the tree rings to generate a ground truth (GT) set of marks, corresponding to the transition between the latewood of ring[*i*] and the earlywood of ring[*i*+1]. These marks delineate the visual

Table 1 Silvicultural practices within each stand for both companies

Age	Lumber company (F)	Density (trees/ha.)	Plywood company (L)	Density (trees/ha.)
0	Plantation in 1995	1111	Plantation in 2002	1000
3	Thinning and pruning to 2.1 m			
4	Thinning and pruning to 4.2 m	666	Thinning and pruning to 1.8 m	533
5			Pruning to 3.4 m	
6			Pruning to 4.5 m	
7	Pruning to 6.4 m		Pruning to 6.4 m	
9	Pruning to 7.2 m			
10	Thinning	450	Thinning	333
14	Thinning	311		

Table 2 The UruDendro dataset

Images corresponding to (a) the lumber company and (b) the plywood company, indicating the image ID code, number of expert traces (marks), number of rings, the year of the earliest annual ring in a given cross-section, and the height and width of the image in pixels

(a) Lumber company						(b) Plywood company					
Code	Marks	Rings	Year	Height	Width	Code	Marks	Rings	Year	Height	Width
F02a	2	23	1996	2364	2364	L02a	1	16	2004	2088	2088
F02b	2	22	1997	1644	1644	L02b	3	15	2005	1842	1842
F02c	4	22	1997	2424	2408	L02c	1	15	2004	1016	900
F02d	2	20	1999	2288	2216	L02d	2	15	2005	921	900
F02e	2	20	1999	2082	2082	L02e	2	14	2006	1914	1914
F03a	2	24	1995	2514	2514	L03a	2	17	2003	2296	2296
F03b	2	23	1996	1794	1794	L03b	2	16	2004	2088	2088
F03c	1	23	1997	2528	2596	L03c	2	16	2006	2400	2416
F03d	1	21	1999	2476	2504	L03d	2	15	2006	2503	2436
F03e	3	21	1998	1961	1961	L03e	2	14	2005	1944	1944
F04a	2	24	1995	2478	2478	L04a	4	17	2003	2418	2418
F04b	1	23	1996	1760	1762	L04b	2	16	2004	1986	1986
F04c	3	21	1998	913	900	L04c	2	16	2005	2728	2704
F04d	2	21	1999	921	899	L04d	2	15	2006	2544	2512
F04e	1	21	1999	2070	2072	L04e	1	15	2005	1992	1992
F07a	1	24	1995	2400	2400	L07a	2	17	2003	2328	2328
F07b	3	23	1996	1740	1740	L07b	2	16	2004	2118	2118
F07c	1	23	1998	978	900	L07c	3	16	2005	2492	2481
F07d	1	22	1999	997	900	L07d	1	15	2006	2480	2456
F07e	1	22	1998	2034	2034	L07e	2	14	2005	1980	1980
F08a	3	24	1995	2383	2383	L08a	2	17	2003	2268	2268
F08b	2	23	1996	1776	1776	L08b	2	16	2004	1836	1836
F08c	2	23	1998	2624	2736	L08c	1	16	2004	2877	2736
F08d	2	22	1998	2388	2400	L08d	2	14	2005	2707	2736
F08e	2	22	1998	1902	1902	L08e	1	15	2005	1666	1666
F09a	1	24	1996	2106	2106	L09a	1	17	2003	1963	1964
F09b	4	23	1996	1858	1858	L09b	3	16	2004	1802	1802
F09c	1	23	1997	2370	2343	L09c	1	16	2005	943	897
F09d	1	23	1997	2256	2288	L09 d	2	15	2006	1006	900
F09e	1	22	1998	1610	1609	L09e	1	15	2005	1662	1662
F10a	2	23	1996	2136	2136	L11b	4	16	2004	1800	1800
F10b	2	22	1997	1677	1677						
F10e	1	21	1998	1800	1800						

transition from darker to lighter zones in the images, when moving from the pith toward the bark (see details in Fig. 2). To do so, they used the Labelme software (Wada 2024), which generates closed polygons formed by vertices positioned by the user over the ring borders throughout its entire circumference. Each closed polygon is a *ring*. The user can place the vertices freely on the image. The definition of a polygon depends on the number of vertices the user defines. The Graphical User Interface supports in-and-out zooming to inspect fine image details. Additionally, polygons can be edited as many

times as needed, even after saving, since the annotation file can be reopened to continue editing.

2.3 Scale calibration

For 40 discs (discs a, b, and e) from the UruDendro dataset, an expert manually measured the ring width (in millimeters) along the north, south, east, and west axes (the black lines in Fig. 3a) using a ruler on the physical wood disc. For the rings traced by the expert on the F02a sample, the distance from the center to the intersection between each ring and the line is shown in Fig. 3b. Each

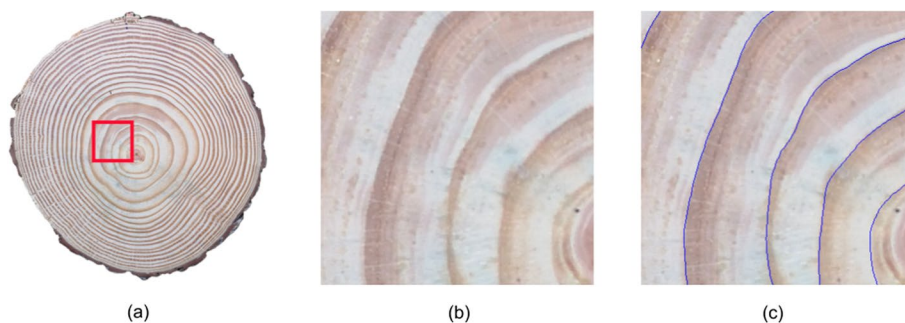


Fig. 2 Accurate manual delineation of tree ring boundaries in images is critical. **a** Wood cross-section image. **b** Zoomed-in view of the red square in **(a)**. **c** The same view with ring mark boundaries in blue

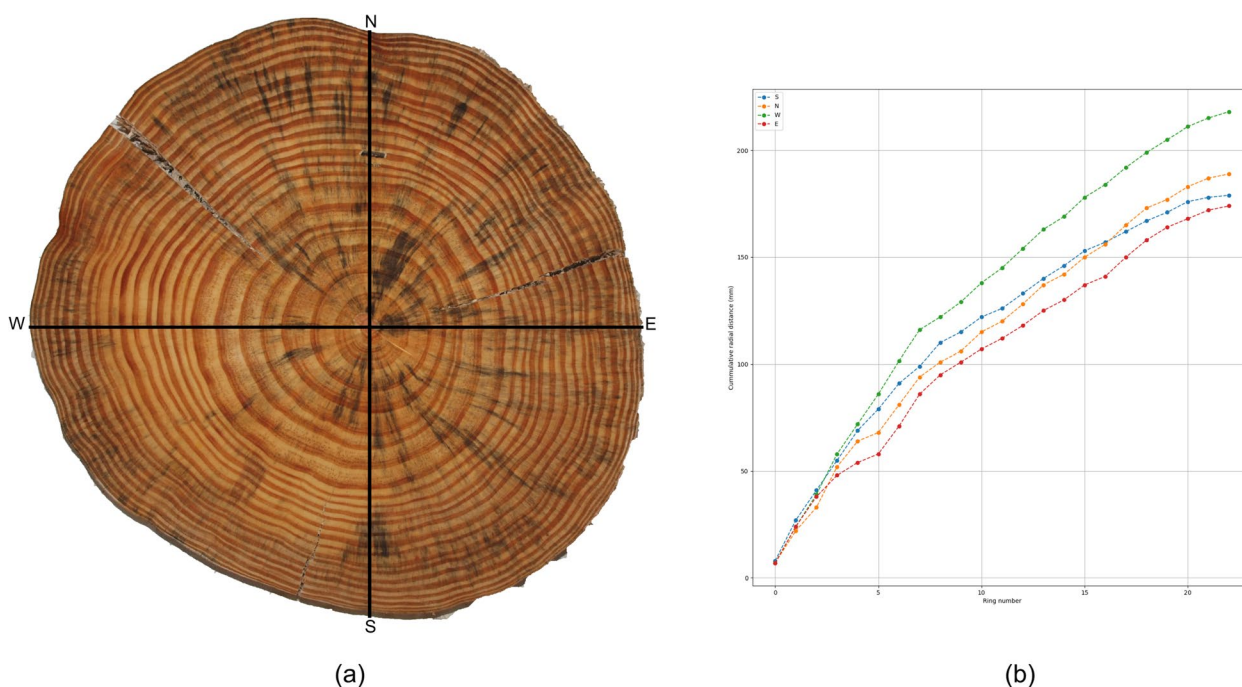


Fig. 3 a Cardinal directions over a tree cross-section (in this case, sample F02a). **b** An expert manually measured ring width along the four black lines corresponding to the cardinal directions, directly on the disc. The South line is blue, the North is orange, the West is green, and the East is red. Measurements, expressed in millimeters, were taken from the center of the disc to the point where each line intersects the tree rings

color corresponds to a different cardinal direction. Additionally, we measured the distance to the pith from the image rings’ annotations (see Sect. 2.2) along the cardinal lines. Therefore, we have the measurements made in the discs (in millimeters), along each direction by an expert, and the measurements made on the same traces on the digital image, in pixels. Assuming a linear model for the relationship between radial distances in millimeters and pixels, we computed the pixel dimensions in millimeters for a given image with expert manual annotations. Equation (1) shows the relation between pixel and millimeter measurements.

$$R_{(mm)} = m * R_{(pixels)} \tag{1}$$

Where $R_{(mm)}$ is the measurement in millimeters along a (horizontal or vertical) direction, $R_{(pixels)}$ is the equivalent measurement but in pixels, and m is a constant that needs to be determined. We estimated the value of the constant m using all the measurements along a given cardinal direction (columns *w_e* and *n_s* in Table 3.a) on a given cross-section or by combining the measurements along several cardinal directions (column *w_{ens}* in Table 3.a).

Table 3 Pixel to millimeter relation

(a) Annual ring width for discs a, b, and e (40 discs) was measured directly from the discs and images in four cardinal directions (north, south, east, and west). The constant m in Eq. (1) is computed by fitting the data by a least squares method using three subsets: all the data (*wens*), data in the West-East direction (*we*), and data in the North-South direction (*ns*). (b) The North-South diameter was measured on discs c and d (24 samples) on the discs and the images. The constant m is computed as the ratio between the measurements made on the discs and those made on the images

(a) Discs a, b and e				(b) Discs c and d	
Code	wens	we	ns	Code	ns
F02a	0.195	0.195	0.194	F02c	0.163
F02b	0.251	0.250	0.252	F02d	0.168
F02e	0.196	0.196	0.197	F03c	0.152
F03a	0.193	0.193	0.193	F03d	0.157
F03b	0.240	0.240	0.240	F04c	0.438
F03e	0.207	0.207	0.208	F04d	0.412
F04a	0.196	0.195	0.196	F07c	0.395
F04b	0.249	0.249	0.249	F07d	0.395
F04e	0.196	0.196	0.196	F08c	0.155
F07a	0.197	0.198	0.196	F08d	0.164
F07b	0.242	0.243	0.242	F09c	0.172
F07e	0.197	0.197	0.197	F09d	0.169
F08a	0.195	0.195	0.194	L02c	0.453
F08b	0.240	0.240	0.239	L02d	0.432
F08e	0.252	0.251	0.252	L03c	0.182
F09a	0.247	0.247	0.247	L03d	0.168
F09b	0.239	0.239	0.239	L04c	0.164
F09e	0.251	0.251	0.250	L04d	0.171
F10a	0.245	0.245	0.245	L07c	0.180
F10b	0.246	0.245	0.246	L07d	0.168
F10e	0.239	0.238	0.240	L08c	0.151
L02a	0.261	0.261	0.261	L08d	0.149
L02b	0.242	0.242	0.242	L09c	0.400
L02e	0.241	0.241	0.241	L09d	0.378
L03a	0.261	0.260	0.261		
L03b	0.259	0.259	0.259		
L03e	0.238	0.238	0.237		
L04a	0.259	0.259	0.259		
L04b	0.259	0.259	0.259		
L04e	0.253	0.258	0.249		
L07a	0.256	0.257	0.256		
L07b	0.256	0.257	0.255		
L07e	0.238	0.238	0.239		
L08a	0.259	0.260	0.259		
L08b	0.259	0.259	0.258		
L08e	0.261	0.261	0.262		
L09a	0.257	0.258	0.257		
L09b	0.260	0.260	0.260		
L09e	0.260	0.260	0.260		
L11b	0.257	0.258	0.257		

Given a data subset (e.g., ring-width measurements made along the North and South direction), for a given cross-section, we obtained the measurements made manually by the expert, X_h , in millimeters, and the measurement computed from the ring annotations by software, X_{sw} , in pixels. The value of m was computed by fitting the data by a least squares method. This method allows the calibration of each image to determine the dimensions in millimeters. We found $\Delta x \approx \Delta y$, indicating that the pixels were almost square-shaped. The values for each image are in Table 3.a.

For the other 24 discs (discs c and d), the diameter North to South was measured directly on the disc, starting from the north mark (seen in the images), passing through the pith, up to the opposite end. A pixel-millimeter relation was computed as usual (Eq. (1)). The value of this constant is presented in Table 3.b.

Finally, using the pixel-to-millimeter information in Table 3, a black scale bar representing 50 mm in each image is drawn in the upper right corner.

2.4 Metric

To evaluate the performance of an automatic detection method for the dataset, we developed a metric based on that proposed by Kennel et al. (2015).

The set of rings detected using an automated method is called dt , and the set of manually made traces (the ground truth GT) is named gt . We assign one detected ring to the corresponding GT one if more than 60%, which is the threshold value used to report results in Table 4, of the dt ring lies within the area of influence of the gt ring. The area of influence of the gt ring is the band defined between half the distance to each adjacent ring (the set of pixels most proximate to gt). If two or more dt rings comply with this condition, the closer ring to the gt is assigned. The distance between rings is measured at specific positions defined by the Nr (360 by default) rays projected from the pith, geometric center of the first-year tree ring, to the bark. Figure 4 illustrates the CS-TRD (Marichal et al. 2023b) automatic ring detection method performance over the samples F03d and F02d. Figure 4a and d show the detections in red and the GT traces in green. The area of influence covers the whole cross-section, as presented in Fig. 4b and e, and the distance between the gt and dt rings is presented in Fig. 4c and f as a colormap. The distance (in pixels) between a detection and a GT ring is defined by Eq. (2).

$$Dist = \sqrt{\frac{1}{Nr} \sum_{i=0}^{Nr-1} (dt_i - gt_i)^2} \tag{2}$$

Table 4 Results of ring detection in the UruDendro data set

TP true positives, FP false positives, FN false negatives. True negatives are zero for all images. P precision, R recall, F F-score. RMSE mean error, in pixels, between ground truth and detected rings. Execution time in seconds

(a) Lumber company									(b) Plywood company								
Code	TP	FP	FN	P	R	F	RMSE	Time	Code	TP	FP	FN	P	R	F	RMSE	Time
F02a	20	0	3	1.00	0.87	0.93	1.50	15.29	L02a	14	1	2	0.93	0.88	0.90	16.95	26.21
F02b	21	1	1	0.96	0.96	0.96	4.02	13.26	L02b	4	2	11	0.67	0.27	0.38	9.41	21.90
F02c	21	0	1	1.00	0.96	0.98	3.76	12.26	L02c	11	0	2	1.00	0.85	0.92	5.33	21.33
F02d	20	1	0	0.95	1.00	0.98	2.11	8.34	L02d	7	3	7	0.70	0.50	0.58	5.66	28.80
F02e	20	1	0	0.95	1.00	0.98	7.62	23.31	L02e	11	0	3	1.00	0.79	0.88	4.92	18.66
F03a	22	2	2	0.92	0.92	0.92	8.11	19.37	L03a	14	0	3	1.00	0.82	0.90	3.45	16.20
F03b	20	0	3	1.00	0.87	0.93	2.15	13.95	L03b	15	1	1	0.94	0.94	0.94	2.22	10.17
F03c	23	0	1	1.00	0.96	0.98	10.69	7.34	L03c	15	1	1	0.94	0.94	0.94	9.01	8.28
F03d	19	1	2	0.95	0.91	0.93	7.81	11.26	L03d	14	0	1	1.00	0.93	0.97	10.63	8.26
F03e	20	2	1	0.91	0.95	0.93	1.66	15.70	L03e	13	0	1	1.00	0.93	0.96	3.97	14.96
F04a	21	1	3	0.96	0.88	0.91	7.71	28.90	L04a	15	0	2	1.00	0.88	0.94	6.21	7.98
F04b	19	0	4	1.00	0.83	0.91	4.60	40.24	L04b	15	0	1	1.00	0.94	0.97	6.35	10.66
F04c	18	1	3	0.95	0.86	0.90	5.60	26.88	L04c	14	0	2	1.00	0.88	0.93	3.30	8.26
F04d	17	3	4	0.85	0.81	0.83	2.90	55.38	L04d	14	1	2	0.93	0.88	0.90	7.88	6.19
F04e	19	2	2	0.91	0.91	0.91	9.94	24.33	L04e	10	1	5	0.91	0.67	0.77	4.09	10.14
F07a	18	1	6	0.95	0.75	0.84	11.68	18.27	L07a	13	1	4	0.93	0.77	0.84	1.89	13.96
F07b	17	3	6	0.85	0.74	0.79	7.99	45.74	L07b	13	0	3	1.00	0.81	0.90	6.56	9.01
F07c	20	2	3	0.91	0.87	0.89	4.85	35.81	L07c	14	1	3	0.93	0.82	0.88	2.41	5.56
F07d	20	0	2	1.00	0.91	0.95	1.04	19.95	L07d	14	0	2	1.00	0.88	0.93	1.73	5.22
F07e	8	4	14	0.67	0.36	0.47	8.17	40.29	L07e	11	0	3	1.00	0.79	0.88	13.26	17.80
F08a	21	1	3	0.96	0.88	0.91	5.28	17.13	L08a	15	0	2	1.00	0.88	0.94	2.38	8.94
F08b	21	1	2	0.96	0.91	0.93	1.72	23.57	L08b	14	1	2	0.93	0.88	0.90	11.99	24.48
F08c	21	1	2	0.96	0.91	0.93	2.05	13.25	L08c	15	0	1	1.00	0.94	0.97	2.52	8.74
F08d	20	0	2	1.00	0.91	0.95	2.10	9.54	L08d	13	0	1	1.00	0.93	0.96	9.57	5.45
F08e	22	0	0	1.00	1.00	1.00	6.70	17.65	L08e	14	1	1	0.93	0.93	0.93	8.14	17.82
F09a	21	0	3	1.00	0.88	0.93	2.20	16.13	L09a	14	0	3	1.00	0.82	0.90	3.29	10.03
F09b	22	1	1	0.96	0.96	0.96	2.91	11.98	L09b	15	1	1	0.94	0.94	0.94	2.26	13.54
F09c	21	0	3	1.00	0.88	0.93	2.83	9.11	L09c	15	2	1	0.88	0.94	0.91	2.90	12.02
F09d	21	0	2	1.00	0.91	0.96	3.44	8.71	L09d	13	1	2	0.93	0.87	0.90	2.12	12.03
F09e	14	5	8	0.74	0.64	0.68	7.08	38.73	L09e	13	0	2	1.00	0.87	0.93	4.14	14.66
F10a	17	1	5	0.94	0.77	0.85	4.24	15.23	L11b	15	1	1	0.94	0.94	0.94	1.54	10.96
F10b	19	2	3	0.91	0.86	0.88	4.75	20.39									
F10e	18	0	2	1.00	0.90	0.95	2.13	12.57									

Where dt_i is the radial distance to the pith of the detection, and gt_i is the radial distance to the pith of the corresponding GT ring, for the same node i .

Once all automatic ring detections are assigned to the GT rings, we calculate the following indicators:

1. True positive (TP): if the detected closed chain is assigned to a GT ring.
2. False positive (FP): if the detected closed chain is not assigned to a GT ring.
3. False negative (FN): if a GT ring is not assigned to any detected closed chain.

Finally, Precision is given by $P = \frac{TP}{TP+FP}$, Recall by $R = \frac{TP}{TP+FN}$ and the F-score by $F = \frac{2P \times R}{P+R}$.

3 Access to data and metadata description

The dataset (Marichal et al. 2023a) is available from the Zenodo Repository at <https://doi.org/10.5281/zenodo.15110647>. The dataset is organized into several files containing the images and marks as described in Table 5.

The **images.zip** file contains one image per sample disc. The **images_no_background.zip** file contains one image without a background per sample disc. Additionally,

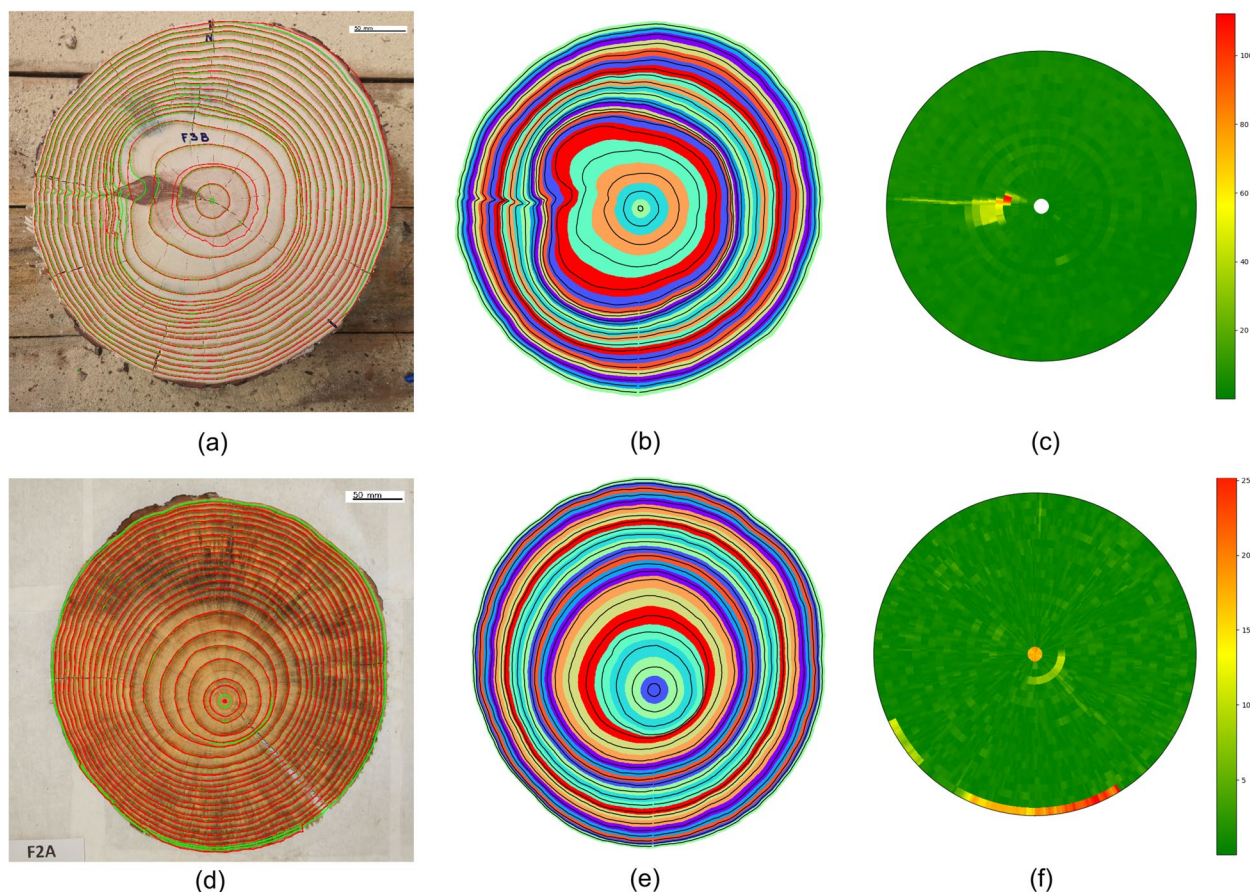


Fig. 4 Measuring the error between automatic detection and human ring annotations for samples F03d (upper row) and F02b (lower row). **a** and **d** Human ring annotations are green; the rings the automatic ring detector produces are red. **b** and **e** Areas of influence of the manual rings (ground truth, GT). **c** and **f** Absolute radial distance, in pixels, between the detection and the GT ring annotations. Table 3 allows for the computation of the error in millimeters

Table 5 File details

Name	Format	Example	Explanation
images.zip	png	F02c.png	Original images
images_no_background.zip	png	F02c.png	Images of disc without background
images_scale_bar.zip	png	F02e.png	Images with a printed scale bar as sample F02a in Fig. 1
ring_annotations.zip	json	F02c.json	Annual ring annotations
pith_location.csv	csv	-	pith pixel position in the image
radial_growth_lumber.ods	ods	-	Radial growth measurements in the lumber company's discs
radial_growth_plywood.ods	ods	-	Radial growth measurements in the plywood company's discs
discs_diameter.csv	csv	-	Diameter measurement from discs c and d
pixel_millimeter.txt	txt	-	Data from Table 3 in txt format

the file **images_scale_bar.zip** includes the images from **images.zip**, each overlaid with a 50-mm scale bar, computed using the calibration factors detailed in Table 3 (see Fig. 1).

There are five different annotation types in the **ring_annotations.zip** file. The file naming convention is as

follows: for file **IMAGENAME-ANNOTATOR.json**, **IMAGENAME** refers to the image sample identification code, and **ANNOTATOR** is the expert who annotated the file, identified by a letter: V, M, S, and C. The file **IMAGENAME.json** contains the average ring annotations among experts. The annotations are presented in json format

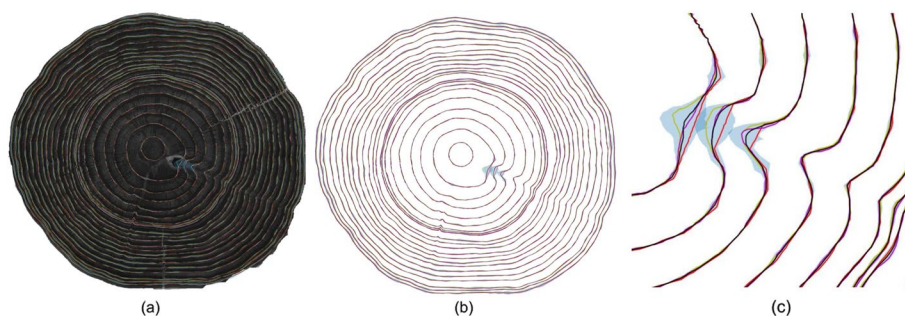


Fig. 5 Manual tracing of image F08a. **a** image with superimposed marks by three experts; **b**) marks, **c**) a detail. Marks by experts are violet, red, and yellow. The mean of the three expert marks is black, and the band in blue is the area spanned by three standard deviations around the mean. Note the variability of the experts tracing

with all the detected rings as a list of shapes of type polygon, each one formed by a list of points in image coordinates (pixels). This *json* file uses the structure defined by Labelme Tool (Wada 2024), defined as follows, not used keys are indicated:

- `imagePath` (string) Optional. Local Path to the image file.
- `imageHeight` (integer) Optional. Image height in pixels.
- `imageWidth` (integer) Optional. Image width in pixels.
- `version` (string). Optional. Software version (not used).
- `flags` (dictionary). Optional. Flags used by the detection with comments (not used).
- `imageData` (string). Optional. String with image matrix stored in hexadecimal (not used).
- `shapes` (list of dictionaries). Required. List of rings. Each element is a dictionary with the following keys.
 - `label` (string). Optional. Ring identifier.
 - `points` (list of pixel coordinates). Required. Each pixel coordinate is a floating-point number. Pixel (x,y) where x refers to the horizontal axis and y to the vertical axis.

The pith data is in file **pith_locations.csv**. It is a table. Indexing by cross-section ID code gives the pixel coordinates of the pith; as a convention, the center occupies one pixel.

The manual measurements described in Section 2.3 are provided in the files **radial_growth_lumber.ods** and **radial_growth_plywood.ods**. For each ring growth year, measurements were taken in the four cardinal directions, as illustrated in Fig. 3. The North-South diameter measurements for discs c and d are provided in **discs_diameter.csv**. File **pixel_millimeter.txt** is the data from Table 3.

4 Technical validation

The database was split among four technicians (researchers, undergraduates, and graduate students), all especially trained but with varying expertise in tree-ring tracing. One to four experts annotated each photograph; the number for each image is detailed in Table 2 (Marks' column), with each expert labeling all the rings visible in the disc. Therefore, we have more than one annotation per tree ring: the mean ring was computed between the different annotations made by experts to obtain one GT ring, as is shown in Fig. 5. A senior expert verified the mean ring for each photograph to consolidate the results (GT data).

5 Reuse potential and limits

This dataset was created to support developing and evaluating computer vision algorithms for detecting annual tree rings in wood cross-section images of the *P. taeda* species.

To illustrate the potential use of the UruDendro dataset, we made the following experiment. We used the UruDendro dataset to train the INBD method proposed by Gillert et al. (2023), developed initially for detecting shrub rings in microscopy images. By doing so, we were able to expand the automatic ring detection of INBD method to process in field-acquired photos, such as those shown in Fig. 6 from the dataset (Longuetaud et al. 2022).

Another potential application is fine-tuning automatic tree-ring detection methods for core images, such as the one proposed by Poláček et al. (2023). This can be achieved by splitting the images in the dataset into patches that follow the format specified by Poláček.

The same dataset has been used to develop an automatic algorithm for pith localization detection (Marichal et al. 2025), as accurate pith localization enables the measurement of growth ring eccentricity.

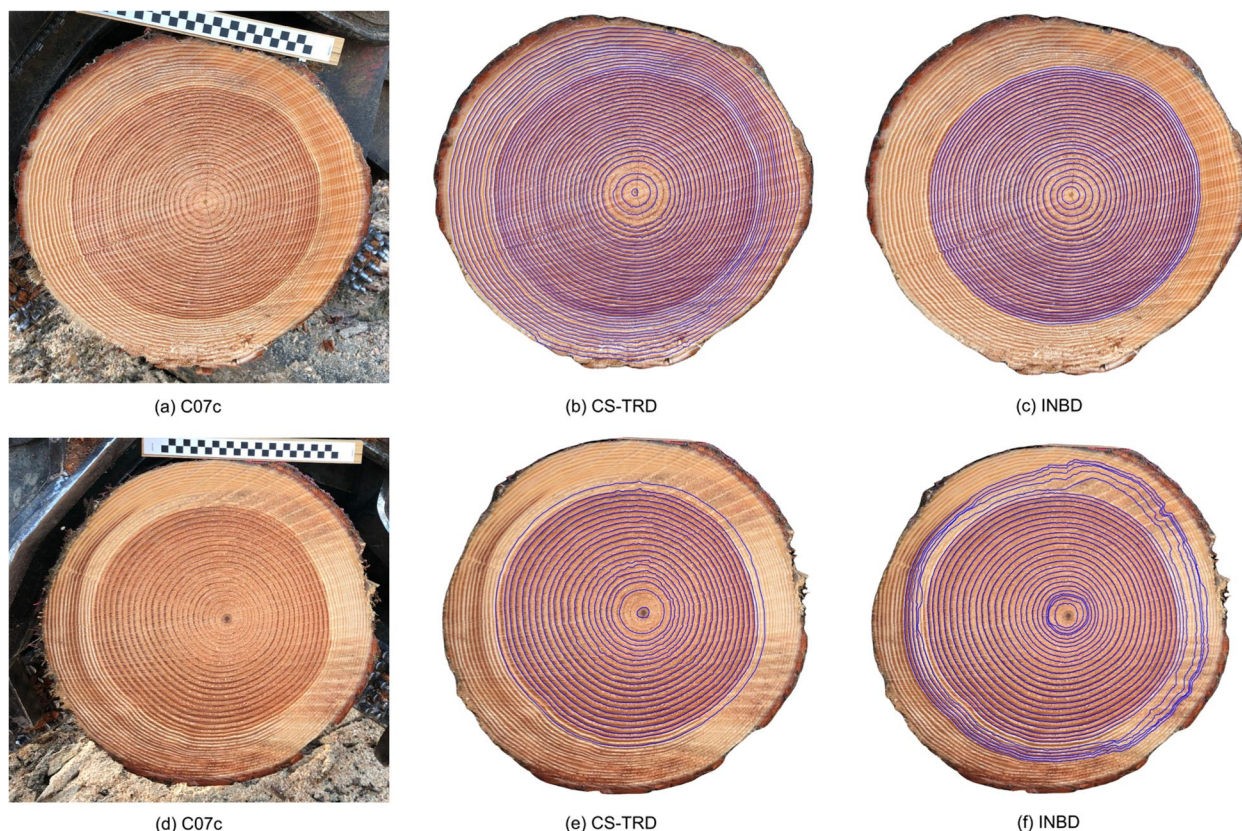


Fig. 6 C07d (first row) and C08d (second row) samples from *Douglas fir* dataset (Longuetaud et al. 2022). Images taken in the field. Comparison between the automatic tree ring detection method CS-TRD and INBD (Gillert et al. 2023)

This dataset can also be used to analyze the combined effect of different silvicultural practices and climate on the growth rates of commercial plantations. The measurements made between 10 cm (images a) and 435 cm (images e) at different tree ages can also be used to evaluate allometric equations and develop tree growth models.

Finally, the availability of the cross-section images and the marks performed by the experts can be used to train and assess the performance of novel technicians devoted to tree ring analyses.

5.1 Visualize annotations

To visually inspect the annotations over an image, a Python GitHub repository is available: <https://github.com/hmarichal93/urudendro>. Annotations can be visualized on the image using the following code:

```
from urudendro.dataset import visualize_annotation
ANNOTATION_FILE = 'path/to/annotation/file'
IMAGE_PATH = 'path/to/image/file'
OUTPUT_PATH = 'path/to/output/directory'
visualize_annotation(ANNOTATION_FILE, IMAGE_PATH, OUTPUT_PATH)
```

Where ANNOTATION_FILE is the path to the annotation file, IMAGE_PATH is the path to the image, and OUTPUT_PATH is the path to write the results.

5.2 Automatic ring detection method comparison

We applied the CS-TRD method to automatically detect the tree rings in the dataset. The third column of Fig. 4 shows the error in pixels between the GT rings and the detected curves by the CS-TRD method assigned to them. The green color represents a low error, while the red represents a high error. For the F03d sample, note that the error is concentrated around a knot in the wood, which perturbs the automatic detection of some rings. These heat maps are constructed with a homogeneous radial distribution of rings, highlighting the error at a given ring and radial direction. While for the F02b sample, there are detection errors in the second detection and in the outermost detection, colored in yellow-red in the heatmap.

The Table 4 illustrates the CS-TRD performance on the UruDendro dataset. All images were resized to 1500×1500 pixels. The average F -score is 89%, the average precision is 95%, and the average recall is 86%. For example, in the image *F03d*, the method failed to detect two GT rings, so $FN = 2$. The other rings were correctly detected. The table also shows the execution time for each image and the RMSE error (Eq. (2)) between the detected and GT rings. The mean RMSE error between GT and detected rings over the entire data set is 5.27 pixels, and the mean execution time for each image was 17.27 s using an Intel Core i5 10300H workstation with 16GB of RAM.

Below is an example of Python code, using the GitHub repository tools to calculate the metrics mentioned in 2.4 for a given image and annotations.

```
from urudendro.metric_influence_area import main as metric

DETECTION_FILENAME = 'path/to/detection/file'
GROUND_TRUTH_FILENAME = 'path/to/ground/truth/file'
IMAGE_FILENAME = 'path/to/image/file'
CX = #x-pith coordinate
CY = #y-pith coordinate
THRESHOLD = 0.6
OUTPUT_DIR = 'path/to/output/directory'

P, R, F, RMSE, TP, FP, TN, FN = metric(DETECTION_FILENAME, GROUND_TRUTH_FILENAME,
    IMAGE_FILENAME, CX, CY, THRESHOLD, OUTPUT_DIR)
```

Where DETECTION_FILENAME is the path and name of the detection file, GROUND_TRUTH_FILENAME is the path to the ground truth file, IMAGE_FILENAME is the path to the image file, CX is the pith x coordinate in pixels, CY is the pith y coordinate in pixels, THRESHOLD is the threshold to consider a detection as valid (between 0 and 1) and OUTPUT_DIR is the path to the results output directory.

5.3 Limitations

The main limitation of this dataset is its relatively small size for training deep learning methods, which typically require hundreds or even thousands of images. However, as illustrated in Fig. 6, training models with this dataset can still support tree-ring detection in images from different domains, such as those acquired in the field.

Acknowledgements

The study is an interdisciplinary collaboration among researchers at Uruguayan institutions: Facultad de Ingeniería, Facultad de Agronomía, CENUR Noreste, and CENUR Litoral Norte, all from Universidad de la República. The companies Grupo Lumin, FYMNSA, Arboreal, Agroempresa Forestal, Global Forest Partnership and Cambium are acknowledged for logistical support during tree harvesting. Fundación Latitud, Forestry Department of Facultad de Agronomía, and the Forestry System of the Instituto Nacional de Investigación

Agropecuaria (INIA) are acknowledged for being part of the experimental design that led to the collection of cross-sections analyzed in this work.

Authors' contributions

Conceptualization: Henry Marichal, Diego Passarella, Christine Lucas, Ludmila Profumo, Gregory Randall; methodology: Henry Marichal, Diego Passarella and Gregory Randall; formal analysis and investigation: Henry Marichal, Christine Lucas, Verónica Casaravilla, Serrana Ambite, and Maria Noel Rocha Galli; writing—original draft preparation: Henry Marichal, Diego Passarella, and Gregory Randall; writing—review and editing: Henry Marichal, Christine Lucas, Diego Passarella, Gregory Randall; funding acquisition: Diego Passarella and Gregory Randall; resources: Ludmila Profumo, Diego Passarella, and Gregory Randall; supervision: Ludmila Profumo, Diego Passarella, and Gregory Randall. The authors read and approved the final manuscript.

Funding

This work was supported by project ANII-FMV-176061: UruDendro 2.0: Aplicación de técnicas de procesamiento de imágenes e inteligencia artificial para la dendrometría automática de especies de madera nativas y comerciales.

Additionally, it was supported by project ANII ART_X_2021_1_170389: Detección temprana de madera de compresión en pino para una mayor eficiencia industrial.

Data availability

The datasets generated during and/or analysed during the current study are available in <https://doi.org/10.5281/zenodo.15110647>. The Python code used is available in <https://github.com/hmarichal93/uruDendro>.

Declarations

Ethics approval and consent to participate

Not applicable.

Consent for publication

All authors gave their informed consent to this publication and its content.

Competing interests

The authors declare that they have no competing interests.

Received: 4 January 2025 Accepted: 29 May 2025

Published online: 01 July 2025

References

Beck HE, Zimmermann NE, McVicar TR et al (2018) Present and future Köppen-Geiger climate classification maps at 1-km resolution. *Sci Data* 5(180214). <https://doi.org/10.1038/sdata.2018.214>

- Fabijańska A, Danek M (2018) Deepdendro - a tree rings detector based on a deep convolutional neural network. *Comput Electron Agric* 150:353–363. <https://doi.org/10.1016/j.compag.2018.05.005>
- Gillert A, Resente G, Anadon-Rosell A et al (2023) Iterative Next Boundary Detection for Instance Segmentation of Tree Rings in Microscopy Images of Shrub Cross Sections. In: Proceedings of the IEEE/CVF Conference on Computer Vision and Pattern Recognition (CVPR). pp 14540–14548. <https://doi.org/10.1109/CVPR52729.2023.01397>
- GIMP tool (2025) Gnu image manipulation program (gimp), version 3.0.2. community, free software (license gplv3). <https://gimp.org/>. version 3.0.2, Free Software. Accessed 06 Apr 2025.
- INIA (2023) Open database: Meteorological data. tacuarembó station. <http://www.inia.uy/gras>. Accessed 06 Apr 2025.
- Kennel P, Borianne P, Subsol G (2015) An automated method for tree-ring delineation based on active contours guided by DT-CWT complex coefficients in photographic images: Application to abies alba wood slice images. *Comput Electron Agric* 118:204–214. <https://doi.org/10.1016/j.compag.2015.09.009>
- Kim D, Ko C, Kim D (2023) Method for detecting tree ring boundary in conifers and broadleaf trees using mask r-cnn and linear interpolation. *Dendrochronologia* 79:126088. <https://doi.org/10.1016/j.dendro.2023.126088>
- Longuetaud F, Pot G, Mothe F et al (2022) Traceability and quality assessment of Douglas fir (*Pseudotsuga menziesii* (Mirb.) Franco) logs: the TreeTrace_Douglas database. *Ann For Sci* 79(46). <https://doi.org/10.1186/s13595-022-01163-7>
- Marichal H, Passarella D, Lucas C et al (2023a) UruDendro, a public dataset of 64 cross-section images and manual annual ring delineations of *Pinus taeda* L. V1. [Dataset]. <https://doi.org/10.5281/zenodo.15110647>
- Marichal H, Passarella D, Randall G (2023b) CS-TRD: a Cross Sections Tree Ring Detection method. arXiv preprint <http://arxiv.org/pdf/2305.10809>. [astro-ph.IM]. Accessed 06 Apr 2025.
- Marichal H, Passarella D, Randall G (2025) Automatic wood pith detector: Local orientation estimation and robust accumulation. In: Antonacopoulos A, Chaudhuri S, Chellappa et al (eds) Pattern Recognition. Springer Nature Switzerland, Cham, pp 1–15
- Poláček M, Arizpe A, Hüther P et al (2023) Automation of tree-ring detection and measurements using deep learning. *Methods Ecol Evol* 14(9):2233–2242. <https://doi.org/10.1111/2041-210x.14183>
- Shi J, Xiang W, Liu Q et al (2019) Mtreering: An r package with graphical user interface for automatic measurement of tree ring widths using image processing techniques. *Dendrochronologia* 58:125644. <https://doi.org/10.1016/j.dendro.2019.125644>
- Wada K (2024) Labelme: Image polygonal annotation with python. <https://doi.org/10.5281/zenodo.5711226>

Publisher's Note

Springer Nature remains neutral with regard to jurisdictional claims in published maps and institutional affiliations.